Role of Honeycomb in Improving Subsonic Wind Tunnel Flow Quality: Numerical Study Based on Orthogonal Grid

Hudhaifa Hamzah[†,‡*], Laith M. Jasim[‡†], Ali Alkhabbaz[‡‡], Besir Sahin[†]

[†] Dept. of Mechanical Eng., College of Eng., Cukurova University, Adana 01330, TURKEY;

[‡] Dept. of Mechanical Eng., College of Eng., University of Mosul, Mosul 41002, IRAQ;

[‡†] Dept. of Mechatronics Eng., College of Eng., University of Mosul, Mosul 41002, IRAQ;

[‡‡] Dept. of Mechanical Eng., College of Eng., Korea Maritime and Ocean University, Busan 49112, SOUTH KOREA.

[*]Corresponding Author Email: hudhaifahamzah@gmail.com

ABSTRACT

In the present study, a numerical analysis of the laminar incompressible flow through an open subsonic wind tunnel is conducted in order to determine the flow quality within the test section. The unsteady two-dimensional governing equations of stream function, ψ and vorticity, ω transport in an orthogonal curvilinear coordinate are solved using the finite difference method (FDM). Flow inside the honeycomb regions within the settling chamber is characterized by using Brinkman–Forchheimer–extended Darcy model with specific properties. The main objective of this study is to select a convenient design of honeycomb structure depending on its porosity, β, and thickness, T_{ho}, that ensures a maximum effective area of the test section with minimum overall power losses through the wind tunnel. The effect of Reynolds number ($500 \leq Re \leq 2000$), honeycomb porosity ($0.85 \leq \beta \leq 0.9825$), honeycomb thickness with respect to the settling chamber length ($0.25 \leq T_{ho} \leq 1$) and various inlet velocity profile on the flow uniformity of the test section and the considerations of power losses are investigated. The findings of this investigation affirmed that the honeycomb porosity has a direct impact on the flow quality testing and power losses throughout the considered wind tunnel.

KEYWORDS

Flow quality, Honeycomb, Orthogonal grid, Porous medium, Subsonic wind tunnel.

INTRODUCTION

Wind tunnel experiments are still necessary to obtain the comprehensive of measurement data needed for detailed design decisions for a wide variety of engineering applications such as estimate the response of buildings and bridges to the wind effects, predicting the wind level speeds of the pedestrian, study of boundary layers development, and geometrically scaled model testing for the full or specific components of aircraft, trains and cars and then verify the numerical results [1]. Despite great progress made in the computational methods in recent years and contrary to past advice, Computational Fluid Dynamics (CFD) has not achieved the desired aim in substituting the wind tunnel, as clearly identified by Meroney et al. [2]. Earlier, the traditional way of dealing with this an engineering design issue has been to utilize a collection of empirical, theoretical, and numerical computations to get an elementary identification. Regardless of the great development in CFD, it can be said that the CFD has reached a stage where a synergistic effect can be generated by direct combination with the wind tunnel approach.

From one side, numerical results such as values of lift, drag and pitching moment, pressure distribution, etc. for different models are validated by comparison with wind tunnel measurements. From the other side, the CFD approach offers a rapid and economical means to support wind tunnel component design, desired flow quality, and matching wind tunnel parts to commercial fans and energy consideration. Therefore, the CFD and the wind tunnel support each other to obtain accurate results with minimum cost. The use of the CFD tool to support various aspects of component design/choice and flow uniformity in the tunnels has been examined by many researchers [3], [4]. For example, A new methodology for numerical simulation of flow conditions in a closed-circuit wind

tunnels has been evolved by Moonen et al. [3] to evaluate the CFD function in wind tunnel measuring and design. It was found that this methodology usually reproduces the wind tunnel measurements of average velocities with an error of 10% or less. In another study, the same authors [4] numerically developed a set of six new complementary indicators to assess the quality of spatial flow in the wind tunnel test sections by using the methodology that developed previously.

The indices showed a detailed visualization of the flow quality in the test section as well as the ability to perform CFD-based design of new wind tunnels. The overall performance of various engineering systems is improved under uniform flow conditions. To achieve this purpose, many flow-resistance devices have been installed within the flow passage. Perforated plates used in electrostatic precipitators or desulphurization tower [5] and multiple screens used in wide-angle diffusers [6] are typical examples of these devices. For instance, Sahin et al. [7] experimentally investigated the affecting parameters of the wire gauzes and perforated plates on the flow control in a wide-angle diffuser. Their results showed that good flow uniformity and pressure recovery could be achieved by using a certain number of wire gauze screens or perforated plates with specific porosities and locations. The conditions for the flow resistance element have been numerically derived by Choi et al. [8] to standardize an arbitrary non-uniform flow in a two-dimensional channel in terms of an irregular porous plate with a uniform thickness. The developed simple formula provides satisfactory results for various velocity profiles at the channel entrance.

By going into the aerodynamic sides of the wind tunnel design: measurements in low-speed facilities, confirmed that low-frequency vorticity fluctuations through the wind tunnel components that generated by the fan were the main source of test section disturbances. The fan blades are designed to suck the fluid in one direction, but it still adds some rotations. Accordingly, flow control is mainly achieved by controlling the separation of the boundary layer and various possible approaches have been applied experimentally to re-straighten the flow, such as installing honeycombs and anti-turbulence screens [9]. Schubauer and Spangenberg [10] conducted one of the earliest experimental studies using screens to check the flow quality of the wide-angle diffusers. They observed that the presence of screens could be prevented or delayed the flow separation in these diffusers depending on their position. Furthermore, Honeycomb has been utilized successfully for many years as a means of straightening and directing airflow for many applications such as air conditioners, ducts, and heaters.

The use of honeycomb panels poses challenges and suspicious for its mathematical model. An alternative approach is to model the honeycomb as a porous material, which means that porous structures were inserted at honeycomb's locations. Unfortunately, few works in the open literature study the flow behavior of honeycomb through wind tunnel numerically. Gordon and Imbabi [11] studied the feasibility of improving the design of many traditional tunnel components by using CFD tests. The mass and momentum equations of the Brinkman model were employed to represent the fluid flow through screens. The momentum equation of the Brinkman model for the porous media was employed to represent the fluid flow through screens. The CFD outcomes showed a crucial role in recognizing the required changes to minimize the size and overall expense of the wind tunnel and produce high-quality flow in the working section. Besides, Kulkarni et al. [12] considered the influence of honeycomb and honeycomb–screen combinations on decreasing the magnitude of vorticity and turbulence level in the test section by computing the governing equations of subsonic flow using the turbulent and porous flow models in a commercially available CFD software package ANSYS-CFX.

The results of these numerical predictions that are related to the effects of honeycombs thickness, cell configurations, and screens of various permeability are detected to be in a suitable consistency with the experimental and theoretical data obtained from the previous works. Fadilah and Erawan [13] using NUMECA software to simulated the influence of screen and honeycomb on flow quality through a wind tunnel. Darcy model for the porous media was utilized to represent the screen and honeycomb. The screen and honeycomb have other applications in thermal power systems such as; air solar systems and thermal storage systems. Group of researchers performed a series of important numerical study [14]–[18] that related in modelized the honeycomb as a porous medium and validates this hypothesis. The topics of thermal and solar energy storage in the presence of a honeycomb had been the general problem in these papers. The Brinkman-Forchheimer-extended Darcy model for the porous media was applied to modelized the honeycomb in Refs. [14], [15], while the Brinkmanr-extended

Darcy model was applied in Refs. [16]–[18], and the numerical investigation of these articles was accomplished by using Ansys-Fluent code.

Finally, they concluded that the porous medium model can be used to modelized the honeycomb and its numerical simulation will be simpler. According to our survey, there are many studies about the flow characteristics through the wind tunnels, but there are no numerical studies that take into account the effect of honeycomb structure on the flow uniformity, effective test section size, and power losses. Also, few numerical studies represented the honeycomb by the models of porous media. In this study, a numerical technique concerning the finite difference method is adapted in orthogonal curvilinear coordinates to simulate the fluid flow through an open subsonic wind tunnel. The momentum equations were modeled as porous media based on the Brinkman-Forchheimer-extended Darcy model for the honeycomb region. This study aims to select an adequate honeycomb structure design that takes into account the effects of porosity and thickness for the honeycomb on the flow uniformity, effective test section size, and energy loss. Further, the significance of this study focuses on building numerical program that provides an accurate representation of the airflow through the wind tunnel and the account of energy losses for each part of the wind tunnel. The results of this CFD program have an effective role for choosing a suitable wind tunnel design and analyzing the configuration effect of each part of the wind tunnel (such as settling chamber, honeycomb, nozzle, diffuser) on the velocity profile through the test section, the effective area of the test section, and power losses.

PROBLEM DESCRIPTION

The low-speed wind tunnel facility considered in this work is an open-circuit type with a small test section (working section) size, which is widely used for research and instructional analyses. Typically, the size of the tunnel depends on its purpose. Wind tunnel components are designed and constructed to ensure that the flow in the test section as close as possible to the irrotational (free-stream) flow conditions. Manuals like those prepared by Metha and Bradshaw [19] provide basic information about the design procedures and required parameters for the proper building of the wind tunnel constructions. Fig. 1 displays the main components of an open subsonic wind tunnel which is used as a model in this study. The essential step in wind tunnel design is to determine the size and shape of the test section according to the type of expected tests. The test section dimensions define the overall wind tunnel dimensions, and then the required power. Depending on the cross-sectional area of a square testing section, A the hydraulic diameter, D_h can be calculated as follows [20]:

$$D_h = 2\sqrt{A/\pi} \tag{1}$$
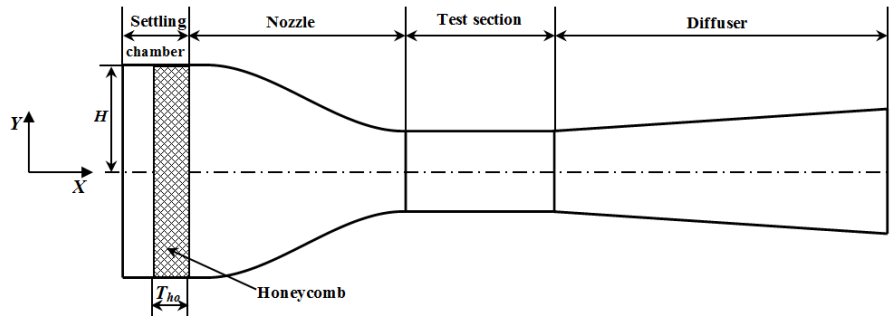
Figure 1. Geometrical schematic of an open-circuit subsonic wind tunnel adapted in this study.

According to the recommendation of Barlow et al. [21], it is better to have the ratio of test section length twice of the hydraulic diameter to have the best flow observation downstream of the tested body. From the specialist article [22], the nozzle entrance/exit typical area ratio was chosen to be 7 over the length equal to the total height ($L_N=2H_i$) of its inlet cross-section. An optimized nozzle wall profiles can have a further reduction in turbulence level and allow a certain degree of temporal velocity stability as well as spatial uniformity in the test section. In the present work, the nozzle wall shape of the fifth-order Bell-Metha polynomial was selected, and its mathematical formulation can be written as follows [22]:

$$y(x) = H_i - (H_i - H_e)[6(\acute{x})^5 - 15(\acute{x})^4 + 10(\acute{x})^3] \tag{2}$$

where $\acute{x}$ is the non-dimensional streamwise distance to the nozzle length. The inlet cross-section area of a typical diffuser is equivalent to the outlet cross-section area of the working section over the length equal to 4 times of its hydraulic diameter and a half angle of 3.5°.

MATHEMATICAL MODEL

Governing equations

The flow field is modeled based on the general transient Brinkman-Forchheimer-extended Darcy equations [23] in the honeycomb region within the settling chamber to demonstrate the inertial and viscous effects, and based on the unsteady Navier-Stokes equations in the fluid domain for the rest of the parts of the wind tunnel. In light of these assumptions, by defining a binary parameter, λ changing from 0 with, $\beta=1$, for the pure Navier-Stokes equation to 1 with, $0.85 \leq \beta \leq 0.9825$, for the porous region. The dimensional governing equations which describe the fluid flow for the current physical problem can be written as:

Continuity equation:

$$\frac{\partial u}{\partial x} + \frac{\partial v}{\partial y} = 0 \tag{3}$$

Momentum equation:

$$\frac{\rho}{\beta^2}\left(\beta\frac{\partial u}{\partial t} + u\frac{\partial u}{\partial x} + v\frac{\partial u}{\partial y}\right) = -\frac{\partial p}{\partial x} + \frac{\mu}{\beta}\left(\frac{\partial^2 u}{\partial x^2} + \frac{\partial^2 u}{\partial y^2}\right) - \lambda\left(\frac{\mu}{K} + \frac{\rho F}{\sqrt{K}}|\mathbf{v}|\right)u \tag{4}$$

$$\frac{\rho}{\beta^2}\left(\beta\frac{\partial v}{\partial t} + u\frac{\partial v}{\partial x} + v\frac{\partial v}{\partial y}\right) = -\frac{\partial p}{\partial y} + \frac{\mu}{\beta}\left(\frac{\partial^2 v}{\partial x^2} + \frac{\partial^2 v}{\partial y^2}\right) - \lambda\left(\frac{\mu}{K} + \frac{\rho F}{\sqrt{K}}|\mathbf{v}|\right)v \tag{5}$$

where $|\mathbf{v}| = \sqrt{u^2 + v^2}$ and F is the Forchheimer coefficient and can be defined as [24]:

$$F = \frac{1.75}{\sqrt{150\beta^3}} \tag{6}$$

In the present study, the characteristic length was taken as the test-section hydraulic diameter. Therefore, the following non-dimensional parameters are introduced to convert the governing equations into a dimensionless form:

$$X = \frac{x}{D_h}, \quad Y = \frac{y}{D_h}, \quad U = \frac{u}{\overline{v}_\iota}, \quad V = \frac{v}{\overline{v}_\iota}, \quad P = \frac{p}{\rho\overline{v}_\iota^2}, \quad \tau = \frac{t\overline{v}_\iota}{D_h} \tag{7}$$

where

$$\overline{v}_\iota = \frac{\int_A \mathbf{v}_i.\mathbf{n}\, dA}{\int_A dA} \quad \text{and} \quad \mathbf{v}_i = u_i i + v_i j.$$

Then the stream function, ψ, and vorticity, ω related to the fluid velocity components are defined as:

$$U = \frac{\partial\psi}{\partial Y}, \quad V = -\frac{\partial\psi}{\partial X}, \quad \omega = \frac{\partial V}{\partial X} - \frac{\partial U}{\partial Y} \tag{8}$$

The momentum Eqs. (4) and (5) are simplified to be one equation by cross-differentiation and then subtracting one from the other. Therefore, the governing equations are transformed into a dimensionless stream function-vorticity equations as follows:

$$\frac{\partial^2\psi}{\partial X^2} + \frac{\partial^2\psi}{\partial Y^2} = -\omega \tag{9}$$

$$\beta\frac{\partial\omega}{\partial\tau} + U\frac{\partial\omega}{\partial X} + V\frac{\partial\omega}{\partial Y} = \frac{\beta}{Re}\left(\frac{\partial^2\omega}{\partial X^2} + \frac{\partial^2\omega}{\partial Y^2}\right) - \lambda\beta^2\left[\omega\left(\frac{F}{\sqrt{Da}}|\mathbf{V}| + \frac{1}{Da\,Re}\right) - \frac{F}{\sqrt{Da}}\left(U\frac{\partial|\mathbf{V}|}{\partial Y} - V\frac{\partial|\mathbf{V}|}{\partial X}\right)\right] \tag{10}$$

Where

$$|\mathbf{V}| = \sqrt{U^2 + V^2}, \quad Re = \frac{\rho\overline{V}_\iota D_h}{\mu} \quad \text{and} \quad Da = \frac{K}{D_h^2}.$$

On the other hand, the pressure differential equation can be written from the motion equations in terms of vorticity, ω as following [25]:

$$\beta^2 \nabla P = -\beta \frac{\partial V}{\partial \tau} - \nabla \left(\frac{|V|^2}{2}\right) + V \times \omega - \frac{\beta}{Re} \nabla \times \omega - \lambda \left(\frac{\beta^2}{Re\,Da} V + \frac{\beta^2 F}{\sqrt{Da}} |V|V\right) \tag{11}$$

Initial and boundary conditions

The initial conditions for unsteady viscous flow development through the wind tunnel can be represented as an impulsive flow that starts from rest. The flow at rest is irrotational and has zeros velocities inside the wind tunnel domain. Therefore, the initial conditions of the stream function, ψ, and vorticity, ω for the wind tunnel domain, Ω are:

$$\omega = \psi = 0 \quad on \ \Omega \ at \ \tau = 0 \tag{12}$$

As the fan draws air from the ambient, certainly the flow at the entrance of the settling chamber has a non-uniform behavior. Thus, one constraint in this study is to choose a nonuniform flow with a high-velocity gradient at the wind tunnel entrance. To acquire these requirements, two different types of velocity profiles were implemented as an inlet boundary condition in this study. One of them is a skewed velocity profile, $U_i = 1.5(Y)^4 + 1.5(Y)^2 + 0.8$, with deviation compared to spatial uniform flow, which is the same as considered in the study of Moonen et al. [4] and Choi et al. [26]. This profile is developed and utilized for most cases in this study. Another one is considered as a special case. Inlet boundary conditions of this special case are presented in Figs. 2 (a), (b), and (c). These profiles were imported from a specific location (where the flow separation occurs) in a wide-angle diffuser connected with an open-circuit wind tunnel during the flow simulation. It is obvious from gradients of the velocity components there is an extremely non-uniform flow. This extremely non-uniform flow exaggerating the real situation that an exemplary wind tunnel faces, however, it could be one of the worst entry situations in a wind tunnel to operate on. At all walls of the wind tunnel in the computational domain, the no-slip boundary condition is adopted. The outflow boundary condition is used at the exit of the diffuser. These boundary conditions are specified as follows:

    i.   Wind tunnel inlet, Γ_i:

$$\psi = YU_i \ , \ \omega = -\frac{\partial U_i}{\partial Y}, \quad at \ \tau > 0 \ \text{ for skewed velocity profile} \tag{13.a}$$
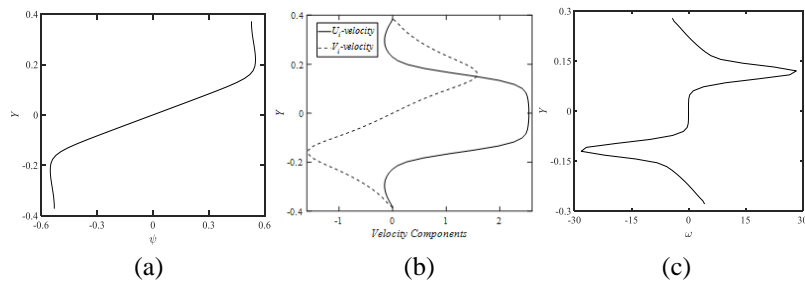
    ii.   Wind tunnel outlet, Γ_e:

$$\frac{\partial \psi}{\partial n} = 0, \ \frac{\partial \omega}{\partial n} = 0, \ P\mathbf{n} = \frac{2}{Re}\frac{\partial \mathbf{V}}{\partial n}, \quad at \ \tau > 0 \tag{13.b}$$

    iii.   The lower wall of the wind tunnel, Γ_{lw}:

$$\psi = -H, \ \frac{\partial \psi}{\partial n} = 0, \ \omega = -\frac{\partial^2 \psi}{\partial n^2}, \quad at \ \tau > 0 \tag{13.c}$$

    iv.   The upper wall of the wind tunnel, Γ_{uw}:

$$\psi = H, \ \frac{\partial \psi}{\partial n} = 0, \ \omega = -\frac{\partial^2 \psi}{\partial n^2}, \quad at \ \tau > 0 \tag{13.d}$$

(a)   (b)   (c)

Figure 2. Exaggerating inlet boundary conditions (special case) of the wind tunnel (a) velocity profile, *U, V*, (b) stream function, ψ, (c) vorticity, ω.

Performance Parameters

The general aerodynamic target for most wind tunnels is to provide a uniform flow within the test section. The current study was interested in investigating the area in which the flow is uniform (irrotational) within the test section, namely the test section effective area. Certainly, the effective area of the test section is less than the geometric area due to the boundary layer region that has nonuniform and rotational flow, also due to other effects. The corresponding criteria that meet the uniform flow requirements are:

$$\omega = 0, \quad \frac{\partial U}{\partial Y} = 0, \quad V = 0 \text{ and } \text{ Boundary layer thickness.} \tag{14}$$

Where boundary layer thickness is the distance from the solid surface to the point in the flow where $u = 0.99U$. To explain the precept of uniform flow distribution through the test section, a criterion on flow uniformity is known as the standard deviation of local velocity distributed over the cross-section within the test section. This was estimated using methods suggested by Sahin et al. [7]. Therefore, the flow uniformity is given as:

$$\sigma_U\% = 100[(U_{rms}/\bar{U})^2 - 1]^{1/2} \tag{15}$$

where $\bar{U}$ is the mean velocity through a cross-section and $U_{rms} = \frac{1}{n}\sum_{i=1}^{i=n} U_i^2$

and n is the number of a cross-section along the test section. An agreeable degree of flow uniformity resembles a value of $\sigma_U\%$ of 30% or less.

The local skin-friction coefficient, C_f at the wind tunnel wall can be expressed as:

$$C_f = -\frac{2\omega}{Re} \tag{16}$$

Another important parameter for characterizing flow through the wind tunnel is the mean pressure recovery coefficient, $\bar{C}_p$, which is defined as follows:

$$\bar{C_p} = \frac{\bar{P_2} - \bar{P_1}}{\frac{1}{2}\bar{\mathbb{V}}_1^2} \tag{17}$$

where

$$\bar{\mathbb{V}} = \frac{\int_A V_i.\mathbf{n}\,dA}{\int_A dA} \text{ and } \bar{P} = \frac{\int_A P\,dA}{\int_A dA}.$$

By applying the law of energy conservation, pressure losses, p_{loss} associated with the flow of fluids in any part of the wind tunnel parts can be obtained as follows [27]:

$$p_{loss} = (P_1 - P_2) + \frac{1}{2}(\varepsilon_1\bar{\mathbb{V}}_1^2 - \varepsilon_2\bar{\mathbb{V}}_2^2) \tag{18}$$

Where

$$\varepsilon = \frac{\int_A \frac{|V|^2}{2}V.\mathbf{n}\,dA}{\frac{\bar{\mathbb{V}}^2}{2}\int_A V.\mathbf{n}\,dA}$$

Then the power losses summation of each section constitutes the total power losses along the wind tunnel:

$$power = \sum(losses \text{ of each section}) \times Q \tag{19}$$

where:

$$Q = \int_A V.\mathbf{n}\,dA \tag{20}$$

ORTHOGONAL GRID GENERATION

357

An effective numerical computation of a set of partial differential equations is directly related to the grid quality. From the perspective of grid quality, well-structured grid that gives an accurate solutions with faster computations should be orthogonal. Therefore, an numerical scheme developed by Eça [28] is proposed for generating an orthogonal grid with control of the boundary point distribution on the present geometry. The scheme is based on an initial algebraic grid that has been achieved by using direct algebraic interpolation to connect the non-uniformly distributed grid points in physical domain (*X-Y* coordinate) to evenly distributed points in the computational domain ($\xi - \eta\ coordinate$).

A two-dimensional orthogonal mapping considered in this study satisfies the following condition:

$$g_{12} = \frac{\partial X}{\partial \xi}\frac{\partial X}{\partial \eta} + \frac{\partial Y}{\partial \xi}\frac{\partial Y}{\partial \eta} = 0 \tag{21}$$

Where g_{12} is the off-diagonal element of the covariant metric tensor. From the above orthogonality condition equation and the Jacobian definition, it is easy to see that the orthogonal mapping satisfies the Beltrami equations:

$$\frac{\partial X}{\partial \eta} = -f\frac{\partial Y}{\partial \xi} \tag{22.a}$$

$$\frac{\partial Y}{\partial \eta} = f\frac{\partial X}{\partial \xi} \tag{22.b}$$

Where *f,* is the distortion function and can be defined as:

$$f = \frac{h_\eta}{h_\xi} \tag{23}$$

and

$$h_\eta = \sqrt{g_{22}} = \sqrt{\left(\frac{\partial X}{\partial \eta}\right)^2 + \left(\frac{\partial Y}{\partial \eta}\right)^2} \tag{24.a}$$

$$h_\xi = \sqrt{g_{11}} = \sqrt{\left(\frac{\partial X}{\partial \xi}\right)^2 + \left(\frac{\partial Y}{\partial \xi}\right)^2} \tag{24.b}$$

The set of covariant Laplace equations used by Ryskin and Leal [29] is easily derived upon eliminating *y* and *x* respectively from Beltrami equations (22):

$$\frac{\partial}{\partial \xi}\left(f\frac{\partial X}{\partial \xi}\right) + \frac{\partial}{\partial \eta}\left(\frac{1}{f}\frac{\partial X}{\partial \eta}\right) = 0 \tag{25.a}$$

$$\frac{\partial}{\partial \xi}\left(f\frac{\partial Y}{\partial \xi}\right) + \frac{\partial}{\partial \eta}\left(\frac{1}{f}\frac{\partial Y}{\partial \eta}\right) = 0 \tag{25.b}$$

For an orthogonal grid generation, equations (25) are solved numerically using Line Successive Over-Relaxation method. An orthogonal computational grid for the wind tunnel is shown in Fig. 3.
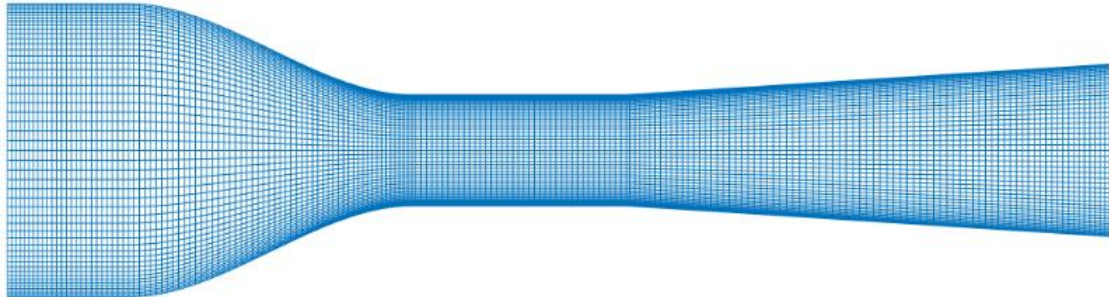

(a) Algebraic grid.

(b) Orthogonal grid.

Figure 3. Mesh configuration with highly packed clustering factor near walls for the considered wind tunnel (a) algebraic, (b) orthogonal.

NUMERICAL SOLUTION

Numerical calculation was done by solving the partial differential equations (Eqs. (9) and (10)) that govern the flow through wind tunnel after converted to the orthogonal form with corresponding initial and boundary conditions. These equations are discretized on an orthogonal body fitted grid by means of finite difference method. Second order central difference scheme is implemented for all the spatial derivative terms, except the convective terms are approximated using the second order upwind scheme in order to stable the numerical solution. The vorticity transport equation (10) is solved using alternating-direction implicit (ADI) scheme with half time-steps to achieve a global truncation error of $O(\Delta\tau^2)$, while the stream function equation (9) is solved using line successive over- relaxation (LSOR) scheme. The obtaining of linear algebraic equations is determined through the tri-diagonal method algorithm (TDMA). As the iteration started, the stream function (ψ) and the vorticity (ω) is calculated for all the nodes in the computational domain. The iteration procedure was repeated until the final convergence criteria for every dependent parameter is less than or equal to 10^{-4}. For all calculations, a time step of 0.001 was utilized. After solving the governing equations, the flow field is obtained which is then used to solve the pressure distribution at each point of computational grid by integrating pressure equations (11) with above mentioned outlet wind tunnel boundary. The program code was written in the MATLAB programming language.

CODE VALIDATION AND GRID INDEPENDENCE TEST

Since there is no experimental data reachable in the open literature for the laminar flow inside a subsonic wind tunnel, the accuracy of the numerical method was verified by simulating the configuration of a two-dimensional diffuser, where the numerical results of three different computational codes are available [30]. The conductance of local mean pressure recovery coefficient, $\bar{C}_{px}$ for low Reynolds number (*Re*=500) along the diffuser was calculated and compared it with the outcomes of Mariotti et al. [30] as depicted in Fig. 4. According to this figure, the predicted values given by the present code are within the acceptable scope for all the computational codes, namely, Fluent, AERO, and Open FOAM.
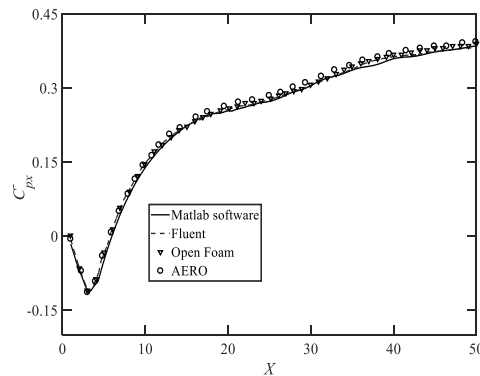
Figure 4. Comparison of the local mean pressure recovery coefficient, $\bar{C}_{px}$ along the diffuser axis for the current code (MATLAB software) with the results of three different codes (Fluent, Open FOAM and AERO) predicted by Mariotti et al. [30] for *Re*=500.

For the sake of grid independence, the velocity profile of the flow at the mid of the test section for $Re=500$, $\beta=0.95$ and $T_{ho}=0.5$ was calculated for grid densities such as (140×51, 210×61, 280×71, 350×81), which is shown in Fig. 5. According to the results, the grid size (280×71) has a good accuracy of the numerical results with accepted running time spent for the computational code and thus is adapted for the rest of the calculation in the present study. The grid clustering factor with highly packed near the wind tunnel wall has been utilized in all cases to capture the best boundary layer attitude.
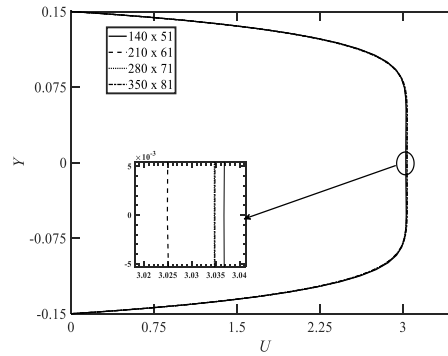
Figure 5. Grid Independence, assigning various mesh distributions that were tested within this study for the velocity profile at the mid of the test section for $Re=500$, $\beta=0.95$ and $T_{ho}=0.5$.

RESULTS AND DISCUSSION

Accessible wind tunnels can be categorized and judged in relation to the intended running ranges of decent flow quality in any facility with respect to any suggested test approach. In this regard, it is clear that poor flow quality conditions can practice such considerable effects on the outcomes of the wind tunnel performance analysis, realizing its origins and management are principally concerned in this study. Perfectly, in the case of an empty test section, the flow within the inviscid flow region along the test section (i.e. flow outside the boundary layers) would be regular and smooth. Because this perfect condition is unreachable in actuality inside the whole geometric test section area due to the effects of the boundary layers, the main question turns of what is the agreeable flow quality at a feasible tunnel efficiency range and consuming power ?.

To understand the flow development through the wind tunnel after the impulsive start (start-up) from rest, the unsteady flows within the time span of $\tau=0.0-100.0$ for $Re=500$ are shown in Fig. 6. This figure presented the time history of the velocity vectors, **V** and vorticity contours, ω through the wind tunnel with and without the honeycomb. These results are obtained with an exaggerating velocity profile (Fig. 2) as an inlet boundary condition for $T_{ho}=1$ and $\beta=0.95$ (in case of with honeycomb). In each longitudinally half of the wind tunnel, it is found that the symmetrical distributions in the flow field are produced, this is due to good design considerations which are adapted for this wind tunnel. Therefore, the presentation is shown only for the longitudinal half of the wind tunnel to give an understandable comparison between the studied cases. Moreover, it was sufficient to stop the program for these cases at the non-dimensional time of $\tau=100$, in which the error value was within the acceptable range, and also there is no remarkable effect on the flow behavior after this time. Generally, the flow development may be divided with the time into three states, namely impulsive start (start-up), transient, and steady (time-asymptotic) state. Fig. 6 showed some selected results within these states. Where the results of $\tau=0.005$ are within the impulsive start state, the results of time span $\tau=0.25$ -25.0 are within the transient state, and the results of $\tau=100$ are within the steady-state.

During the impulsive start state ($\tau=0.005$), the non-uniform flow profile starts impulsively at the inlet of the settling chamber. After this location, it is seen that the distribution of velocity vectors, **V** are nearly uniform and homogeneous (irrotational flow) for the same section along with the remaining parts of the wind tunnel, this occurrence of flow structures is due to the potential flow that considered as an initial condition. The velocity vectors, **V** show there are no clear effects of the honeycomb on the flow during the impulsive start state inside the wind tunnel. With time advancing ($\tau=0.25$-25) during the transient state flow, it can be seen that the development of the boundary layer along the tunnel walls is completed for both cases (with and without honeycomb). At the beginning of the transient state (for both cases), a pair of vortices were generated in the settling chamber as a

result of the inlet velocity profile. In the case of without honeycomb, the intensity and size of these vortices increase with time until they cover the settling chamber and more than the first half of the nozzle at the end of the transient state (τ=25). But in the case with honeycomb, there is no vortex formation through the nozzle and the effect of exaggerating inlet velocity occurs within the settling chamber limits. At steady state (τ=100), it is shown that the honeycomb prevented the vortices expansion and reserve it within the settling chamber.

As expected from the vorticity, ω perspective (right side of Fig. 6), the trend of vorticity function, ω is proportional to the velocity vector, $\mathbf{V}$ of the fluid particle, which is described as twice the angular velocity at a certain point in a flow domain i.e. Thus, $\omega = \nabla \times \mathbf{V}$. The vorticity function, ω gradually decreases over time and starts to spread towards the center of the wind tunnel, and this is related to the formation of the boundary layer. However, it can be noted that the concentration of the vorticity function, ω occurs adjacent to the walls for both cases (with and without honeycomb). When time expires (τ=100), the maximum vorticity magnitudes are accumulating at the exit regions of the nozzle nearby the wall. Eventually, the honeycomb played an important role in vanishing vortices concentrations that formed in the settling chamber and the first half of the nozzle compared to the case without the honeycomb. Therefore, this leads to reducing the vorticity magnitudes in the test section, which gives a larger effective area for examination.
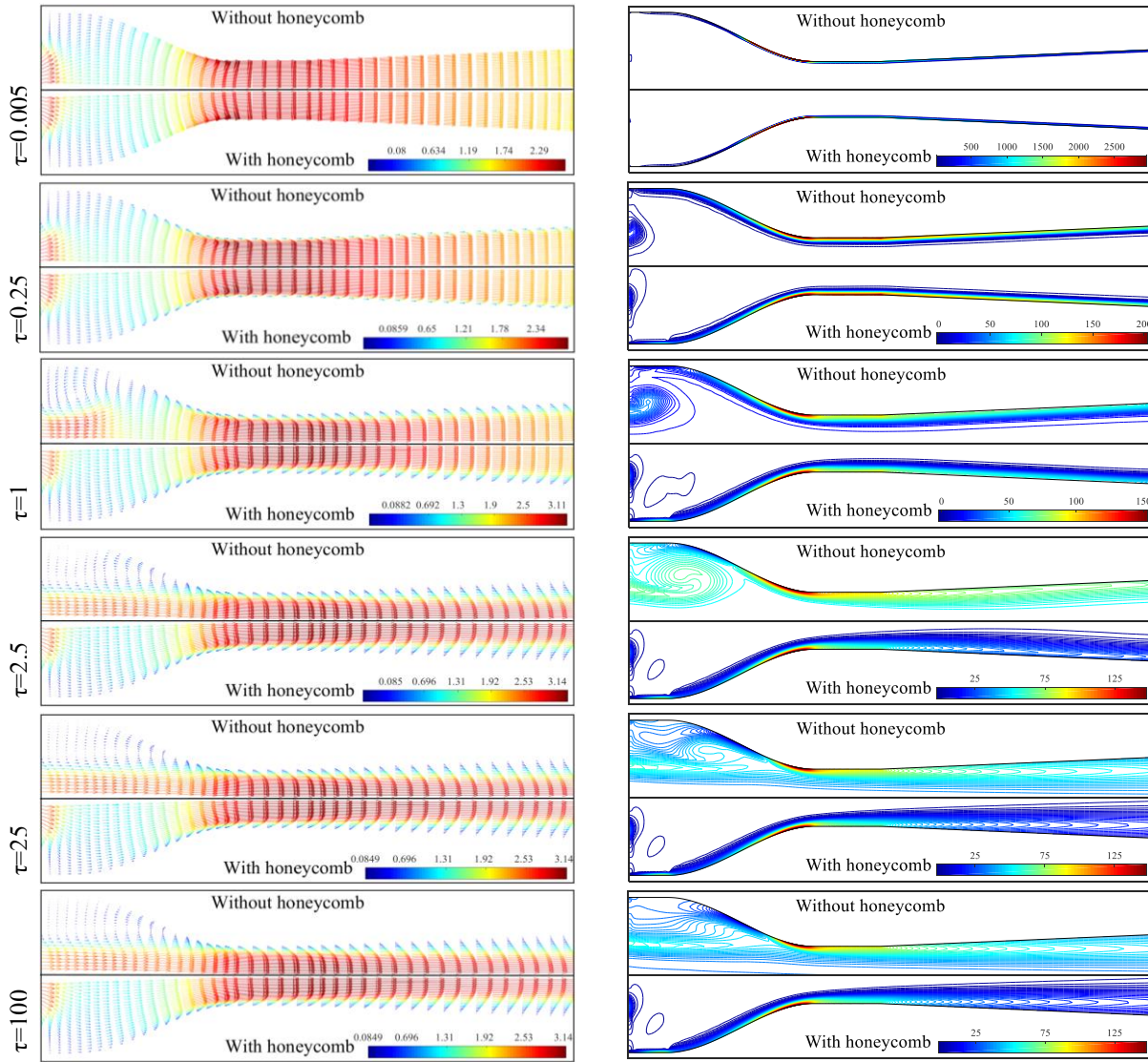

Figure 6. Development of velocity vectors, $\mathbf{V}$ (left) and vorticity, ω contours (right) with time, under an exaggerating velocity profile (special case) for Re=500, β=0.95 and T_{ho}=1 with (lower half of wind tunnel) and without (upper half of wind tunnel) honeycomb cases.

Figure 7 shows the effective area within the test section based on the conditions mentioned in Figure 2 for both special cases that are presented in Figure 6. The ratio of the effective area of the wind tunnel to the total area of the test section with and without the honeycomb is 45.43% and 19.54%, respectively, where there is a free-stream flow zone required for bluff body experiments. However, It can be seen that the honeycomb played an important role in increasing the effective area, but there is also an increase in power losses as distinguished with the outcomes of without honeycomb case. These losses with and without honeycomb are 3.84 and 1.472 respectively.
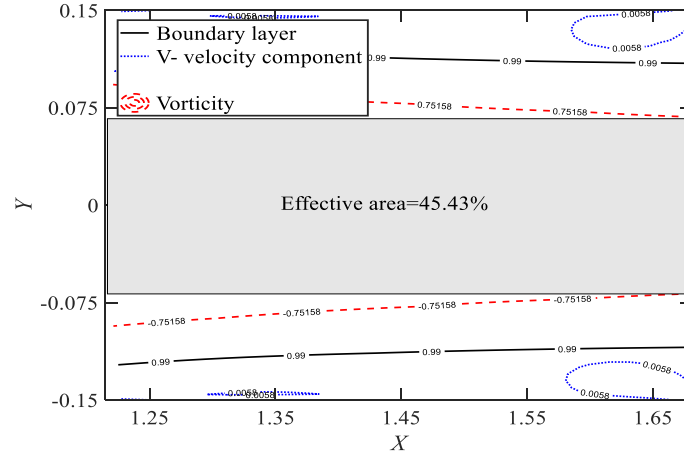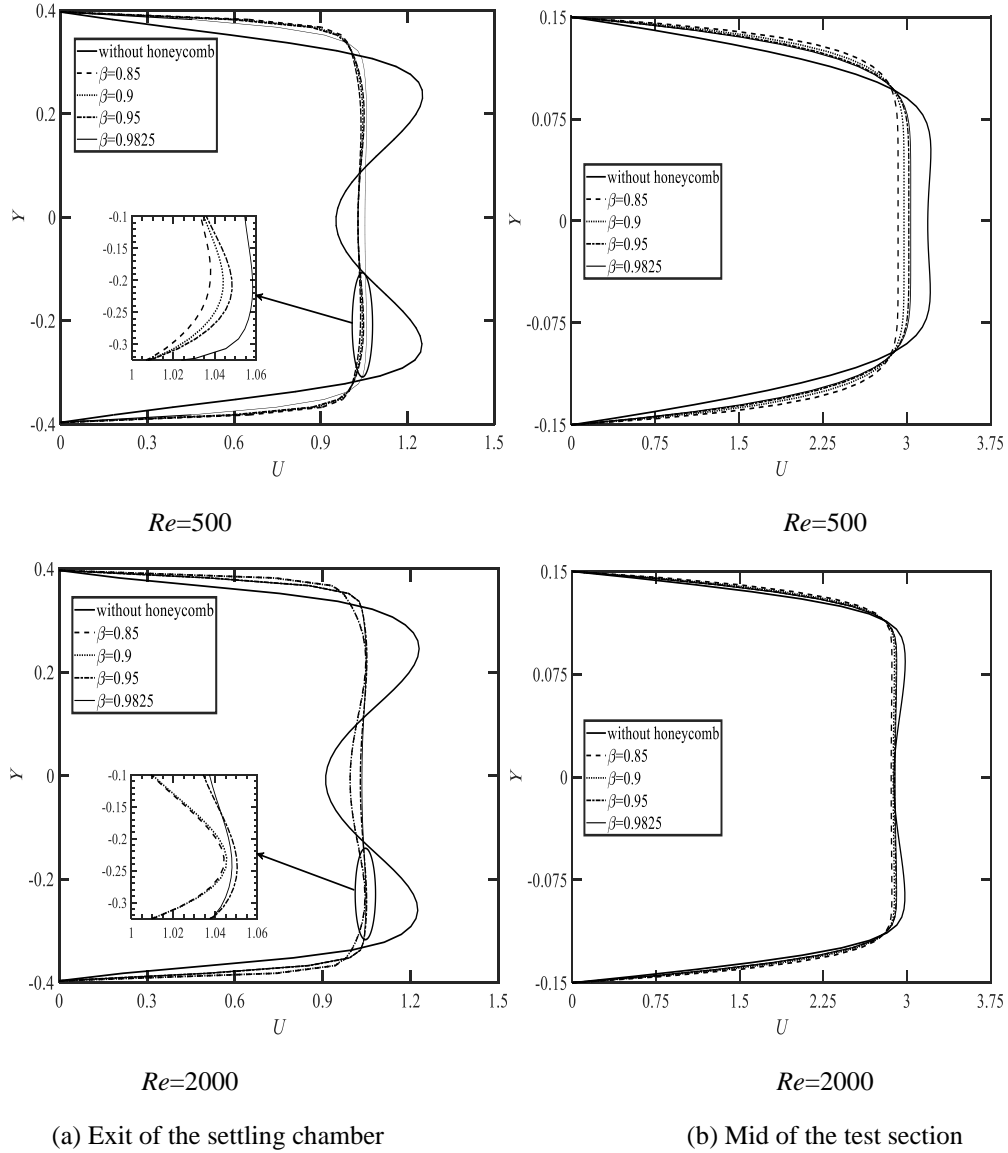

(a) With honeycomb
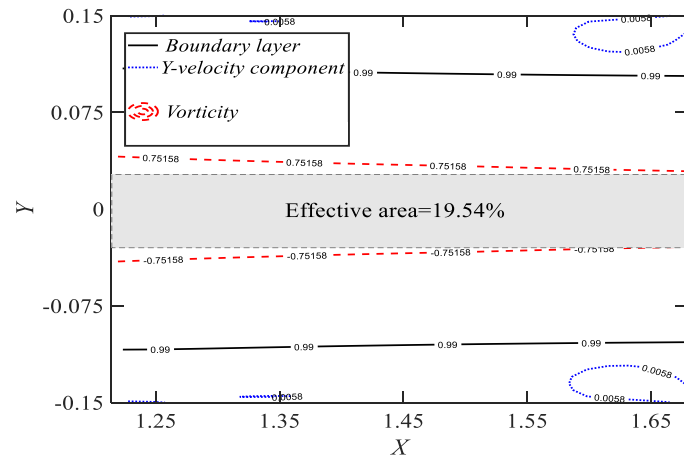
(b) Without honeycomb.

Figure 7. Effective area within the test section for the considered cases in Fig.6 at the steady state (τ=100) for
Re=500 (a) with honeycomb for β=0.95 and T_{ho}=1, (b) without honeycomb.

Figs. 8 (a) and (b) depict the comparison of the velocity profile with and without honeycomb obtained at the outlet of the settling chamber and the midpoints of the test section, respectively, for *Re*=500 and *Re*=2000. In the case of honeycomb existence, the condition of T_{ho} =0.5 for all honeycomb porosities, β is considered. It is clearly noted that the flow after passing through the honeycomb becomes nearly uniform and the flow behaviors and magnitudes seem very similar, while the flow in the absence of honeycomb seems to be unaffected by the settling chamber length. It is noteworthy to mention that the configuration of the fifth-order nozzle improves the uniformity of skewed flow throughout the test section in the absence of honeycomb significantly, but its still not enough for achieving the desired free-stream flow quality. For all examined cases, the magnitude of the velocity in the working section has almost tripled and its profile becomes more uniform as a result of nozzle contraction. In the mid of the test section, it can be observed that the velocity gradients at walls for the case with honeycomb, and thus the wall shear stress, increases as honeycomb porosity, β decreases. In general, the inviscid flow region increases with an increase of the velocity gradient at the walls. The topology of flow patterns depends on Reynolds

numbers, *Re* too, so when the *Re* increases from 500 to 2000 the flow above the wall boundary layer increases and becomes more uniform and consequently, the peak value of velocity decreases slightly.


Re=500   *Re*=500

Re=2000   *Re*=2000

(a) Exit of the settling chamber   (b) Mid of the test section

Figure 8. Effect of porosity, *ß* on the velocity profile for *Re*=500 and *Re*=2000 at the (a) exit of the settling chamber and (b) mid of the test section.

Figures 9 (a) and (b) depict the honeycomb length effect with various Reynolds numbers, *Re* on the velocity profile for constant porosity, *ß*=0.95 at the exit of the settling chamber, and mid of the test section respectively. As shown, the non-uniformity of the inlet velocity profile is significantly improved at the end of the settling chamber when the honeycomb length increases. However, the improvement of the velocity profile was diminished with the increasing of the Reynolds number, *Re*. In the cases of honeycomb exist, it is clearly seen that the velocity profiles at the test section become nearly identical regardless of honeycomb thickness, T_{ho}. This outcome is certainly a consequence of the perfect nozzle configuration design. Moreover, as can be seen from Figs 8 and 9, the nozzle configuration is adequate to enhance the flow quality to an acceptable level in case of inlet velocity with near uniformity.

(a) Exit of the settling chamber (b) Mid of the test section
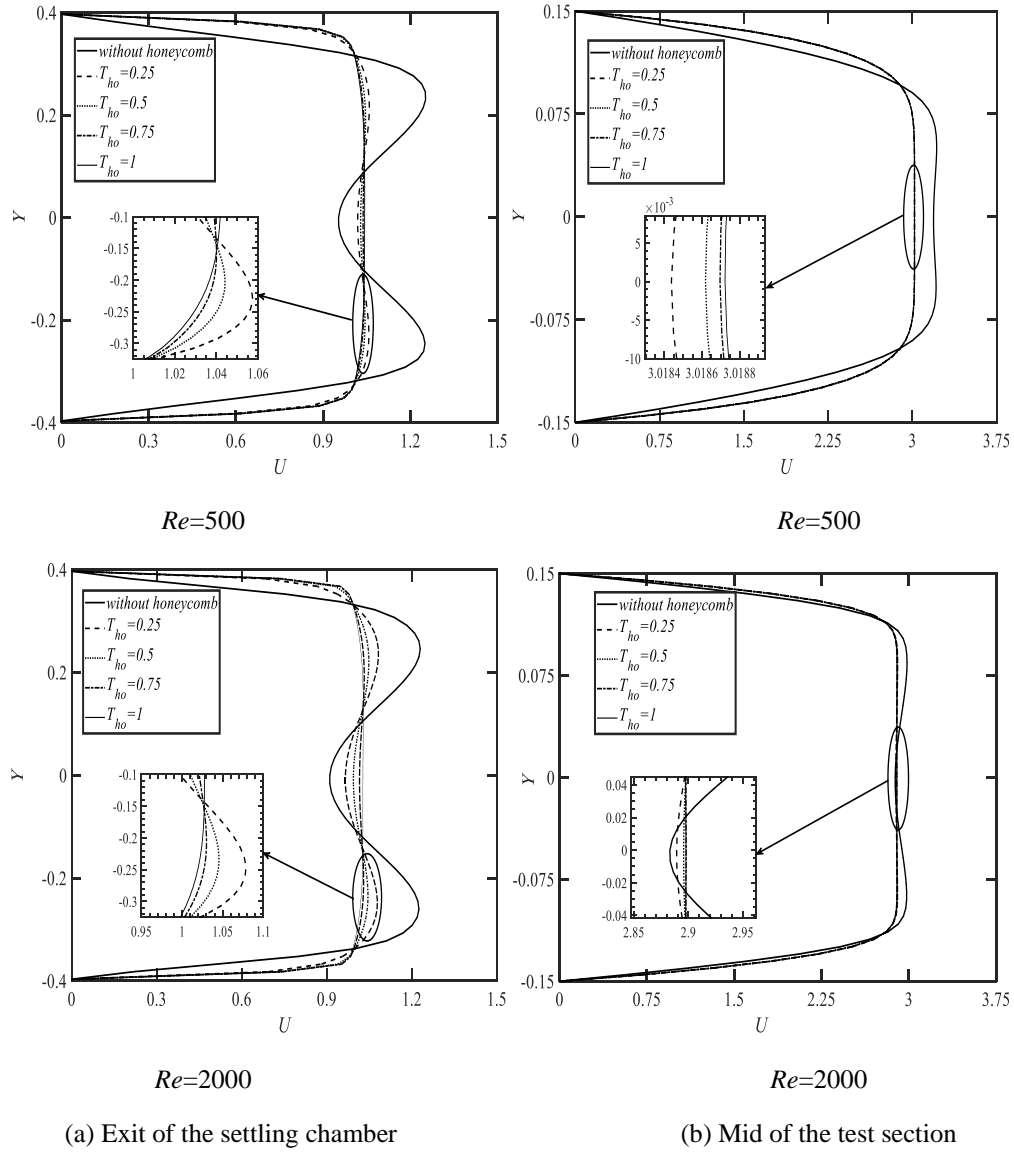
Figure 9. Effect of honeycomb thickness, T_{ho} on the velocity profile for Re=500 and Re=2000 at the (a) exit of the settling chamber and (b) mid of the test section.

The local skin friction coefficient, C_{fx} distribution along the upper wall of the wind tunnel is illustrated in Fig.10 with varied honeycomb porosities and constant thickness T_{ho}=0.5 at (a) Re=500 and (b) Re=2000, respectively. The same trend is observed for all cases considered in this investigation except the case without honeycomb, there is a distinction in the settling chamber. As seen, the local skin friction, C_{fx} is strongly affected by the presence of honeycomb in the settling chamber and then decreases sharply through the nozzle, becomes nearly constant in the test section, and finally starts increasing throughout the diffuser. It is obvious that the values of skin friction distribution are higher in the absence of honeycomb. But, in the presence of honeycomb, these values decrease as the honeycomb porosity, β decreases. However, there is no significant decrement through the settling chamber and nozzle. Furthermore, it is observed that the local skin friction, C_{fx} increases with an increase in Reynolds numbers, Re.
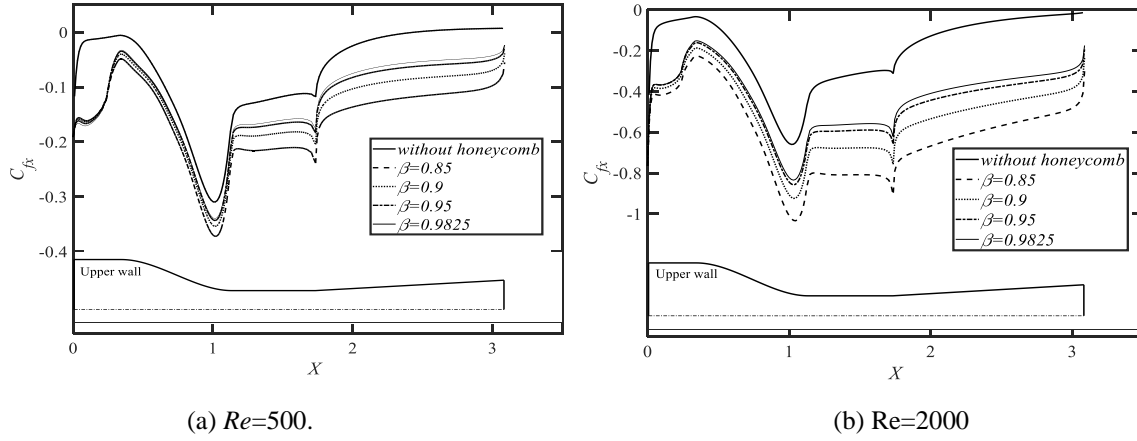
(a) *Re=500.* (b) Re=2000

Figure 10. Local skin friction coefficient, C_{fx} distributions along the upper wall of the wind tunnel for varies honeycomb porosities, β and $T_{ho}=1$ at (a) *Re=500*, (b) *Re=2000*.

Figure 11 shows the local mean pressure coefficient, $\bar{C}_{px}$ distribution along the upper wall of the wind tunnel for various honeycomb porosities and fixed honeycomb thickness $T_{ho}=0.5$ at (a) *Re=500* and (b) *Re=2000*. The pressure coefficient development displays that the flow has an almost zero pressure gradient through the settling chamber followed by an adverse pressure gradient for all the remaining parts of the wind tunnel. Since there is a variation in the surface of the wind tunnel and accordingly a variant in mean velocity, the gradients of the pressure distributions before and after the test section are different. It is clear that the distributions through the settling chamber and nozzle for both Reynolds numbers, *Re* have the same trend with a small difference that exists between cases tested in this study. As the flow enters the test section, the trend of pressure profiles is completely different. For the same *Re*, we can observe that the local pressure coefficient, $\bar{C}_{px}$ for the case of a clear settling chamber is quite close to the prediction to the cases with honeycomb installation in the settling chamber at different porosities.
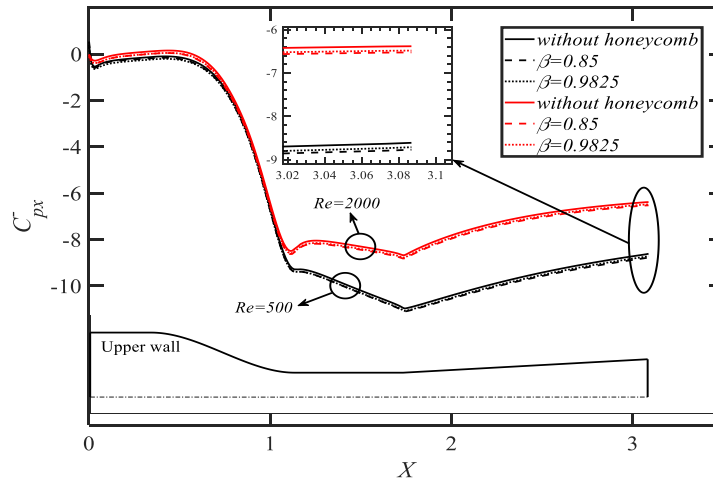
Figure 11. Local mean pressure coefficient, $\bar{C}_{px}$ distributions along the upper wall of the wind tunnel for varies honeycomb porosities, β and $T_{ho}=0.5$ at *Re=500* and *Re=2000*.

Figure 12 represents the pressure losses in a currently designed wind tunnel by splitting the tunnel into component parts with ($\beta=0.95$ and $T_{ho}=0.5$) and without using honeycomb for different Reynolds numbers, *Re*. By comparing the losses with each component, the highest-pressure losses occur in the diffuser and it is followed by the test section, nozzle, and settling chamber, respectively. Accordingly, the total pressure losses through the wind tunnel for the honeycomb existence case are always larger than without the honeycomb case. The effect of the honeycomb existence on the pressure losses is significant for the settling chamber and nozzle while for the other parts is not obvious. For example, the increment in the pressure losses for the settling chamber and nozzle was found to be about 42% and 6% respectively compared to the case without the honeycomb. But there is very little

difference in pressure losses for the test section and diffuser. For all the cases examined in this figure, as the Reynolds number, *Re* increases, we notice that the pressure losses are decreased for each part of the wind tunnel.
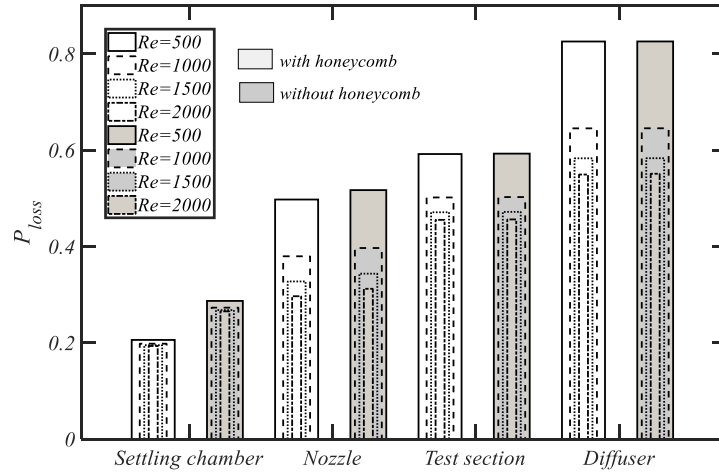
Figure 12. Pressure losses of each part of the wind tunnel with (β=0.95 and T_{ho}=0.5) and without honeycomb for different Reynolds number, *Re*.

Figure 13 illustrates the average power losses of the wind tunnel as a function of the Reynolds number, *Re* for different honeycomb porosities, β, and without the honeycomb. According to the figure, the decrease in power losses is very similar to that with honeycomb vs. without honeycomb. For a given *Re*, the power losses increases as the value of porosity decreases, and the mean increment ratios in comparison with no honeycomb existence case are roughly 6%, 7%, 9%, and 12% for the honeycomb porosities of β =0.9825, β =0.95, β =0.9, and β =0.85 respectively. The effect of decreasing porosities from 0.9825 to 0.95 is very small, indicating that the complexity of additive manufacturing of honeycomb structures with very high porosities has no enough justification in terms of energy consumption. Moreover, the results show that the power losses decrease as the Reynolds number, *Re* increases for all cases.
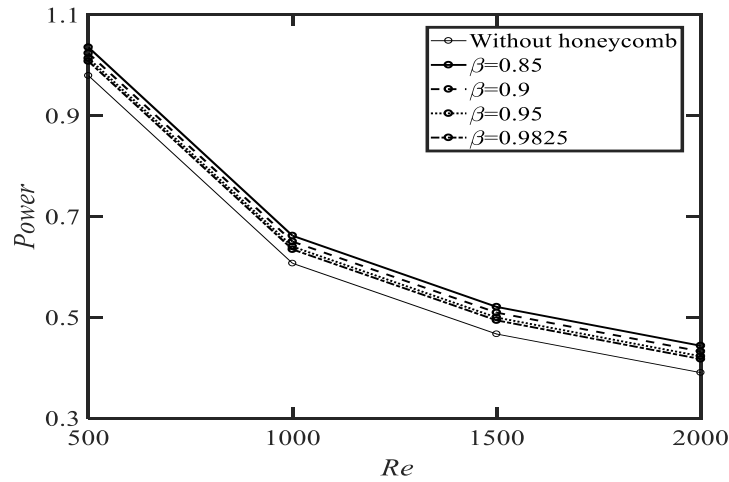
Figure 13. Power losses of the wind tunnel for different honeycomb porosities, β, and various Reynolds number, *Re*.

Figs. 14 shows the variation of the flow uniformity σ_U%, within the test section with Reynolds number, *Re* for different honeycomb porosities, β and without honeycomb case. It can be clearly noted that, for a given *Re*, the flow quality within the test section is more uniform with the lower honeycomb porosity, β. The superiority established by decreasing the honeycomb porosity, β is more pronounced when the allowed Reynolds number is low (i.e. *Re*=500). Anyhow, the gap between honeycomb porosity of β =0.9825 and β =0.95 is comparatively smaller than those between β =0.95 and β =0.9 or β =0.9 and β =0.85, this tendency is in similarity with the power losses presented in Fig. 13. This reveals that the enhancement of flow quality distribution is limited when the

honeycomb porosity, β is increased to a certain value of porosity. Furthermore, in the case of Re=500, the maximum improvements of the flow uniformity over the case of without honeycomb are approximately 37%, 30%, 24%, and 22% for the honeycomb porosity of β =0.85, β =0.9, β =0.95, and β =0.9825, respectively, and the improvement factor is smaller with the increasing of the Reynolds number, Re.
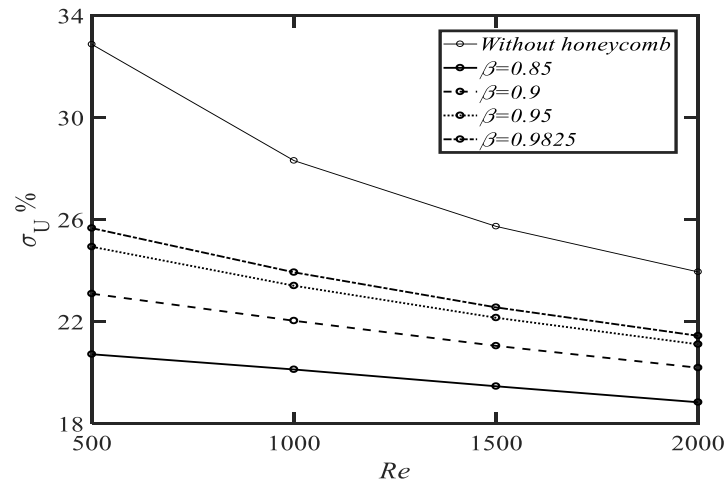
Figure 14. Flow uniformity within the test section for different honeycomb porosities, β, and for various Reynolds number, Re.

CONCLUSION

Fluid flow through an open subsonic wind tunnel under specific inlet velocity profiles was analyzed in this study. The honeycomb region within the settling chamber was considered as a porous medium. Honeycombs with various thicknesses, T_{ho} and porosities, β are investigated. The essential results of the present work can be summed up as follows:

1. The generation and use of an orthogonal grid contribute to reducing the numerical cost of fluid flow simulation.
2. Honeycomb played an important role in preventing the growth and movement of vortices toward the test section.
3. For the disturbance inlet flow, the effective area within the test section increased from 19.54% to 45.43% by using a honeycomb.
4. The presence of honeycomb leads to reducing the vorticity, ω values, and expansion of the irrotational flow region within the test section, which improves the flow quality of the wind tunnel.
5. The flow quality at the exit of the settling chamber is independent of the honeycomb thickness, T_{ho} for the considered porosities, β.
6. Fifth-order nozzle configuration significantly improves the uniformity of skewed flow throughout the test section in the absence of honeycomb, but its still not enough for achieving the desired free-stream flow quality.
7. Decreasing the honeycomb porosity, β causes an increase in power losses and leads flow uniformity, σ_U% enhancement.
8. Flow uniformity, σ_U% is a strong function of Reynolds number, Re. As Reynolds number, Re increases, flow uniformity, σ_U% also increases.
9. The maximum enhancement of the flow uniformity, σ_U% over the case of without honeycomb in this study is 37% at Re=500 and β =0.85.

REFERENCES

[1] G. Ocokoljić, B. Rašuo, and M. Kozić, "Supporting system interference on aerodynamic characteristics of an aircraft model in a low-speed wind tunnel," Aerosp. Sci. Technol., vol. 64, pp. 133–146, 2017, doi: 10.1016/j.ast.2017.01.021.

[2] Meroney Robert N., Leitl Bernd M., Rafailidis Stillianos, and Schatzmann Michael, "Wind-tunnel and numerical modeling of flow and dispersion about several building shapes," J. Wind Eng. Ind. Aerodyn., vol. 81, pp. 333–345, 1999.

[3] P. Moonen, B. Blocken, S. Roels, and J. Carmeliet, "Numerical modeling of the flow conditions in a closed-circuit low-speed wind tunnel," J. Wind Eng. Ind. Aerodyn., vol. 94, no. 10, pp. 699–723, 2006, doi: 10.1016/j.jweia.2006.02.001.

[4] P. Moonen, B. Blocken, and J. Carmeliet, "Indicators for the evaluation of wind tunnel test section flow quality and application to a numerical closed-circuit wind tunnel," J. Wind Eng. Ind. Aerodyn., vol. 95, no. 9–11, pp. 1289–1314, 2007, doi: 10.1016/j.jweia.2007.02.027.

[5] B. Şahin and A. J. Ward-Smith, "Flow control by perforated plates using a blanking technique in wide-angle diffusers employed in practical electrostatic precipitator systems," J. Wind Eng. Ind. Aerodyn., vol. 37, no. 3, pp. 269–284, 1991, doi: 10.1016/0167-6105(91)90012-L.

[6] A. J. Ward-Smith, D. L. Lane, A. J. Reynolds, B. Sahin, and D. J. Shawe, "Flow regimes in wide-angle screened diffusers," Int. J. Mech. Sci., vol. 33, no. 1, pp. 41–54, 1991, doi: 10.1016/0020-7403(91)90026-Y.

[7] B. Şahin, A. J. Ward-Smith, and D. Lane, "The pressure drop and flow characteristics of wide-angle screened diffusers of large area ratio," J. Wind Eng. Ind. Aerodyn., vol. 58, no. 1–2, pp. 33–50, 1995, doi: 10.1016/0167-6105(95)00018-M.

[8] M. K. Choi, Y. B. Lim, H. W. Lee, H. Jung, and J. W. Lee, "Flow uniformizing distribution panel design based on a non-uniform porosity distribution," J. Wind Eng. Ind. Aerodyn., vol. 130, pp. 41–47, 2014, doi: 10.1016/j.jweia.2014.04.003.

[9] B. Sahin and A. J. Ward-Smith, "The pressure distribution in and flow characteristics of wide-angle diffusers using perforated plates for flow control with application to electrostatic precipitators," Int. J. Mech. Sci., vol. 35, no. 2, pp. 117–127, 1993, doi: 10.1016/0020-7403(93)90070-B.

[10] G. Schubauer and W. Spangenberg, "Effect of screens in wide-angle diffusers," 1949, [Online]. Available: http://ntrs.nasa.gov/search.jsp?R=19930082270.

[11] R. Gordon and M. S. Imbabi, "CFD simulation and experimental validation of a new closed circuit wind/water tunnel design," J. Fluids Eng. Trans. ASME, vol. 120, no. 2, pp. 311–318, 1998, doi: 10.1115/1.2820650.

[12] V. Kulkarni, N. Sahoo, and S. D. Chavan, "Simulation of honeycomb-screen combinations for turbulence management in a subsonic wind tunnel," J. Wind Eng. Ind. Aerodyn., vol. 99, no. 1, pp. 37–45, 2011, doi: 10.1016/j.jweia.2010.10.006.

[13] P. A. Fadilah and D. F. Erawan, "Effect of applying screen and honeycomb to the flow characteristic in wind tunnel based on CFD simulation," J. Phys. Conf. Ser., vol. 1130, no. 1, 2018, doi: 10.1088/1742-6596/1130/1/012008.

[14] A. Andreozzi, B. Buonomo, O. Manca, and S. Tamburrino, "Transient analysis of heat transfer in parallel squared channels for high temperature thermal storage," Comput. Therm. Sci., vol. 7, no. 5–6, pp. 477–489, 2015, doi: 10.1615/ComputThermalScien.2016015327.

[15] A. Andreozzi, B. Buonomo, O. Manca, and S. Tamburrino, "Thermal energy storages analysis for high temperature in air solar systems," Appl. Therm. Eng., vol. 71, no. 1, pp. 130–141, 2014, doi: 10.1016/j.applthermaleng.2014.06.036.

[16] A. Andreozzi, B. Buonomo, D. Ercole, and O. Manca, "Phase change materials (PCMs) in a honeycomb system for solar energy applications," Int. J. Heat Technol., vol. 35, no. Special Issue 1, pp. S472–S477, 2017, doi: 10.18280/ijht.35Sp0164.

[17] A. Andreozzi, B. Buonomo, D. Ercole, and O. Manca, "Solar energy latent thermal storage by phase change materials (PCMs) in a honeycomb system," Therm. Sci. Eng. Prog., vol. 6, pp. 410–420, 2018, doi: 10.1016/j.tsep.2018.02.003.

[18] A. Andreozzi, B. Buonomo, D. Ercole, and O. Manca, "Investigation on latent thermal energy storage with parallel squared channel systems," Multiph. Sci. Technol., vol. 30, no. 2–3, pp. 121–134, 2018, doi: 10.1615/MultScienTechn.2018024847.

[19] R. D. Mehta and P. Bradshaw, "Design Rules for Small Low Speed Wind Tunnels.," Aeronaut. J., vol. 83, no. 827, pp. 443–449, 1979.

[20] J. D. Pereira, "Wind tunnels: Aerodynamics, models and experiments," Wind Tunnels Aerodyn. Model. Exp., pp. 1–227, 2011.

[21] and A. P. Barlow, J.B., W.H. Rae Jr, "Low Speed Wind Tunnel Testing.," INCAS Bull., vol. 7, no. 1, p. 33, 2015.

[22] J. H. Bell and R. D. Mehta, "Contraction Design for Small Low-Speed Wind Tunnels.," Jt. Inst. Aeronaut. Acoust. (Technical Report) JIAA TR, 1988.

[23] K. Vafai and C. L. Tien, "Boundary and inertia effects on flow and heat transfer in porous media," Int. J. Heat Mass Transf., vol. 24, no. 2, pp. 195–203, 1981, doi: 10.1016/0017-9310(81)90027-2.

[24] K. Khanafer and K. Vafai, "Isothermal surface production and regulation for high heat flux applications utilizing porous inserts," Int. J. Heat Mass Transf., vol. 44, no. 15, pp. 2933–2947, 2001, doi: 10.1016/S0017-9310(00)00336-7.

[25] T. E. Tezduyar, J. Liou, and D. K. Ganjoo, "Incompressible flow computations based on the vorticity-stream function and velocity-pressure formulations," Comput. Struct., vol. 35, no. 4, pp. 445–472, 1990, doi: 10.1016/0045-7949(90)90069-E.

[26] M. K. Choi, M. K. Cho, H. W. Lee, H. Jung, and J. W. Lee, "Generalized equation for the design of a baffle to generate arbitrary flow velocity profiles," J. Wind Eng. Ind. Aerodyn., vol. 149, pp. 30–34, 2016, doi: 10.1016/j.jweia.2015.11.013.

[27] B. R. Munson, D. F. Young, and T. H. Okiishi, "Fundamentals of fluid mechanics," Fundam. fluid Mech., 1994, doi: 10.1201/b15874-3.

[28] L. Eça, "2D Orthogonal grid generation with boundary point distribution control," J. Comput. Phys., vol. 125, no. 2, pp. 440–453, 1996, doi: 10.1006/jcph.1996.0106.

[29] G. Ryskin and L. G. Leal, "Orthogonal mapping," J. Comput. Phys., vol. 50, no. 1, pp. 71–100, 1983, doi: 10.1016/0021-9991(83)90042-6.

[30] A. Mariotti, A. N. Grozescu, G. Buresti, and M. V. Salvetti, "Separation control and efficiency improvement in a 2D diffuser by means of contoured cavities," Eur. J. Mech. B/Fluids, vol. 41, pp. 138–149, 2013, doi: 10.1016/j.euromechflu.2013.03.002.